An optimal XBT-based monitoring system for the South Atlantic Meridional Overturning Circulation at 34°S

Marlos Goes[1,2] * , Gustavo J. Goni[2], and Shenfu Dong[1,2]

[1] *CIMAS, University of Miami, Miami, FL, United States*

[2] *PHOD, NOAA/AOML, Miami, FL, United States.*

* *Corresponding author:* Marlos Goes, Cooperative Institute for Marine and Atmospheric Studies, Rosenstiel School of Marine and Atmospheric Science, University of Miami, 4600 Rickenbacker Causeway, Miami, FL, 33149,

E-mail: mgoes@rsmas.miami.edu and marlos.goes@noaa.gov .

ABSTRACT

The South Atlantic is an important pathway for the inter-basin exchanges of heat and freshwater with strong influence on the global meridional overturning stability and variability. Along the 34°S meridian, a quarterly, high resolution XBT transect (AX18) samples the temperature structure in the upper ocean, and has been shown to be a useful component of a meridional overturning monitoring system of the region. However, an optimal design for an XBT-based system has not yet been developed. Here we use a high-resolution ocean assimilation product to simulate an XBT-based observational system across the South Atlantic. The sensitivity of the meridional heat transport, meridional overturning circulation, and geostrophic velocities to key observational assumptions is studied. Key assumptions taken into account are horizontal and temporal sampling of the transect, salinity and deep temperature inference, as well as the level of reference for geostrophic velocities. We use the results obtained by the state estimation under observational assumptions to make recommendations for the potential improvements in the AX18 transect implementation.

1. Introduction

The Atlantic Ocean circulation is ubiquitous for having a deep convection site at high latitudes in the northern hemisphere, which drives in large extent the meridional overturning circulation (AMOC) and, therefore, the northward heat transport to the northern latitudes. The variability of the AMOC circulation is responsible for changes in the northern hemisphere climate and may impact the climate globally (e.g., Zhang and Delworth 2005). Despite the high control of the AMOC strength and variability in the North Atlantic Subpolar gyre, the deep convection regions between the Greenland-Iceland-Scotland seas are highly sensitive to heat and freshwater transported from the South Atlantic (Rahmstorf 1996; Donners and Drijfhout 2004), which is suggested to be one of the main drivers of two stable states of the AMOC (Weijer et al. 1999; Beal et al. 2011; Hawkings et al. 2011; Garzoli et al. 2012).

The South Atlantic is a source and sink of heat and mass, with important contributions from fluxes from other basins through, for example, the Agulhas current region (Goni et al. 1997) and the Brazil-Malvinas confluence region (Gordon 1986; Wainer et al. 2000; Goni and Wainer 2001; Goni et al. 2011). The South Atlantic Ocean has been historically one of the least observed regions in the globe; however, several efforts to measure long-term variability in the basin have been put forward in the last decade. For instance, expendable bathythermograph (XBT) observations from the high-density XBT transect AX18 (Figure 1a) measures temperature in the upper 800 m of the ocean four times a year along 34°S. Based on the AX18 XBT data, studies have shown that the mean AMOC and heat transport at 34°S are mostly geostrophically driven, although the wind-driven Ekman component equally contributes to the variability of the meridional transports (Dong et al. 2009). Compensation between the Ekman and geostrophic components may translate in a small annual cycle of heat and volume transports (Garzoli and Baringer 2007; Dong et al. 2009), although models generally do not reproduce this characteristic (Dong et al. 2011).

Currently, observational estimates rely on several assumptions to estimate the integral flow in the South Atlantic. Thus far, only study (Baringer and Garzoli 2007) has estimated the uncertainty resulting from the underlying XBT-based observational system methodological assumptions to measure heat transport across 34°S. However, no sensitivity tests have yet been performed to optimize the sampling strategy in order to maximize the information content, and to assess the uncertainty in volume and heat transports associated with observational and computational methodologies across 34°S. To accomplish this, current high resolution ocean reanalyses can be useful to assess and investigate potential improvements the sampling strategy of the AX18 transect using observing system simulations methodologies. Similar methodologies have been applied, for example, in several studies in the North Atlantic (e.g. Hirschi et al. 2003; Baehr et al. 2004, 2008) to evaluate strategies for monitoring the MOC in the North Alantic.

The aim of the present study is to assess how observational and computational methodologies affect the estimates of volume and heat transports across 34°S in Atlantic Ocean, and how to optimize the design of the AX18 XBT transect in order to reduce uncertainty estimates. Therefore, this study will address four main objectives to evaluate the AX18 XBT transect:

i) The optimal spatial (longitudinal) resolution.

ii) The **optimal** temporal sampling to capture the seasonal variability of the AMOC in the region.

iii) The uncertainties derived from the salinity and deep temperature estimation.

iv) Potential improvements on the assumptions made on the level of reference to resolve the barotropic mode.

To address these goals, we will first describe the characteristics of the region of study (Section 2). We will use a high-resolution global assimilation model (Section 3) that compares reasonably well with the regional observations. and characteristics presented in Section 2. We will define the methodology (Section 4) to calculate volume and meridional heat transport across 34°S, and perform controlled experiments in the model framework to answer point-by-point the above questions (Section 5). Finally, we will discuss the results and make recommendations for the improvement of the AX18 XBT transect measurements (Section 6).

2. Regional characteristics

The subtropical South Atlantic is characterized by a large scale anticyclonic feature, the South Atlantic subtropical gyre (Stramma and England 1999). In the southwestern Atlantic, the surface dynamics is dominated by the Brazil-Malvinas Confluence, which is characterized by the cold northward flow of the Malvinas current, and a southward flowing warm weak western boundary current, the Brazil Current. This region exhibits complex frontal motions (Goni et al. 2011; Goni and Wainer 2001) and patterns with the simultaneous presence of warm and cold rings and eddies (Lentini et al. 2006) and, therefore, characterized by large values of eddy kinetic energy (Figure 1a). In the southeastern Atlantic, the transfer of warm waters from the Indian Ocean into the South Atlantic subtropical gyre largely takes place in the form of rings and filaments formed when the Agulhas Current retroflects south of Africa between 1°W and 25°E (Goni et al. 1997). The eastward flowing South Atlantic current and the northward flowing Benguela current complete the circulation, delimiting the southern and eastern boundaries of the subtropical gyre, respectively. The Brazil-Malvinas Confluence region and the Agulhas retroflection region represent the most energetic areas covered in the region of study. These two regions present similar values of mean eddy kinetic energy, above 1000 cm^2 s^{-2} (Figure 1a), as observed by the altimetric sea level anomalies (Ducet et al. 2000) for the

2007-2012 time period. The Brazil-Malvinas Confluence and Agulhas retroflection regions are both crossed by the XBT transect AX18 (Figure 1a).

3. The HYCOM-NCODA reanalysis

As suggested in previous studies, the strong mesoscale energy in the South Atlantic region requires a minimum of eddy-permitting models to resolve its main features (Treguier et al. 2007; Biastoch et al. 2009). In the present study we use data from the Hybrid Coordinate Ocean Model (HYCOM)-Navy Coupled Ocean Data Assimilation (NCODA) assimilative product (Chassignet et al. 2009), encompassing a total of nearly 6 years of model simulation, sampled in a 7-day timestep using 7-day averages. We combine three experiments, numbered as GLBa0.08/74.2 (June 2007 to September 2008), GLBa0.08/expt_90.6 (September 2008 to May 2009), GLBa0.08/expt_90.8 (May 2009 to May 2013) in order to be to maximize the temporal coverage of the model output.

The HYCOM-NCODA is configured for the global ocean with HYCOM 2.2 as the dynamical model. Computations are carried out on a Mercator grid between 78°S and 47°N, with an average of 1/12° ($\sim$ 7 km) horizontal spacing and 32 vertical layers. A bipolar patch is used for regions north of 47°N. Bathymetry is derived from the U. S. Naval Research Laboratory 2-minute DBDB2 (Digital Bathymetric Data Base) dataset. Surface forcing is from the Navy Operational Global Atmospheric Prediction System (NOGAPS) and includes 3-hourly and 0.5° wind stress, wind speed, heat flux (using bulk formula), and precipitation. The NCODA methodology (Cummings 2005) uses the model forecast as a first guess in a multi-variate Optimal Interpolation (MVOI) scheme and assimilates available along-track satellite sea height anomaly observations (obtained via the NAVOCEANO Altimeter Data Fusion Center), in-situ sea surface temperature (SST), as well as available in-situ vertical temperature and salinity profiles from XBTs, ARGO floats and moored buoys. MODAS synthetic profiles are used by NCODA for downward projection of surface information (Fox et al. 2002).

Compared to altimetric observations, the eddy-resolving HYCOM-NCODA reanalysis reproduces reasonably the main circulation features of the region (Figure 1b). The output of this model, however, shows lower energy in the Brazil-Malvinas Confluence and Agulhas retroflection regions (Figure 1c). Low biases are generally on the order of -300 cm^2 s^{-2} or lower, which is also observed in the comparison of the sea level root-mean square variability of the region (Figure 2a, b). We select 18 realizations (Figure 2a) of the AX18 transect based on the criteria of being zonally directed (median angle $< 10°$ and close to the mean section (between 30° and 36° of latitude) to compare the model thermohaline behavior with the actual XBT observations along the nominal 34°S **define criteria**. Below 850 m, the maximum depth sampled by

the XBTs, the WOA05 annual climatology (Locarnini et al. 2006) is used. The mean temperature section retrieved by the AX18 along the nominal of 34°S shows an east-west gradient, with higher temperatures in the west (Figure 2b, c). The associated zonal density gradients allow an average geostrophic volume and heat transports to the north, as shown in previous studies (e.g., Ganachaud and Wunsch 2003; Garzoli and Baringer 2007). The model shows generally negative temperature biases in the interior ($\sim$ 1 to 2°C) and positive biases on the boundaries ($\sim$1 to 1.5 °C) relative to the mean AX18 section above 850 m , and stronger stratification on the bottom of the ocean in comparison to the WOA05 climatology (Figure 2g-i).

4. Methodology

This study focuses on the reconstruction of the AMOC streamfunction (PSI_y) and the heat transport (HT) along 34°S by simulating XBT observations. This section describes how the AMOC and HT are defined through the paper.

a. AMOC

The AMOC streamfunction is defined as:

$$PSI_y(z) = \int_{x_E}^{x_W} \int_{z}^{-H} v(x,z)dxdz \tag{1}$$

i.e., the integral of the meridional velocity v(x,z) from the bottom (H) to the depth (z) of the ocean and between the western (x_W) and the eastern (x_E) boundaries of the basin. The meridional velocity v(x,z), and therefore its derived meridional streamfunction, can be decomposed into three dynamical components (Lee and Marotzke 1998):

$$v(x,z) = \frac{1}{H}\int_{-H}^{0} v(x,z)dz + [v_E(x,z) - \frac{1}{H}\int_{-H}^{0} v_E(x,z)dz] + v_{sh}(x,z) \tag{2}$$

where the first term on the right hand side of Equation (2) is known as the barotropic or gyre component (v_{bar}), which is here defined as the local average of v(x,z) over the depth H of the ocean, the second term is the Ekman component compensated by a depth-independent flow, and the last term is the vertical shear component, which consists of the velocities calculated using the thermal wind relationship. Other ageostrophic contributions (frictional and non-linear) are not defined. v_E is derived from the local zonal wind stress (τ_x):

$$v_E = -\frac{\tau_x}{\rho_0 f D_E} \tag{3}$$

where ρ_0 = 1025 kg m^{-3} is the mean water density, f the Coriolis parameter, and D_E is the depth of the Ekman layer, which is arbitrarily assumed here to be D_E = 50 m (e.g., Pond and Pickard 1983).

The barotropic and vertical shear velocities combined constitute the absolute geostrophic velocity, which is estimated using the dynamic method assuming a reference level (Pond and Pickard 1983). Barotropic velocities have strong contribution to the geostrophic flow at locations of sloping topography, and their projection on the AMOC can therefore be an important term in the AMOC reconstruction (Baehr et al. 2004).

b. Meridional Heat Transport

The meridional heat transport is calculated as follows:

$$HT = \rho_0 c_p \int_{-H}^{0} \int_{x_E}^{x_W} v(x,z)\theta(x,z)dxdz - \rho_0 c_p M_y \langle\theta\rangle \tag{4}$$

where $c_p = 4187$ J kg^{-1}K^{-1} is the specific heat of the sea water, and $\langle\theta\rangle$ is the averaged potential temperature θ along the section. The second term in Equation (4) is a constraint to allow zero mass transport across the section, which is necessary for heat transport calculations in free surface models, since they do not necessarily have zero mass transport at any given time period (Jayne and Marotzke 2001; Griffies et al. 2004).

To reconstruct HT, Equation (4) is further decomposed into the same components as the meridional overturning, using the corresponding decomposition of the velocity (Equation 2). Following (Hall and Bryden 1982):

$$HT = \rho_0 c_p \int_{-H}^{0} \int_{x_E}^{x_W} v_{bar}\theta_{bar}dxdz + \int_{-H}^{0} \int_{x_E}^{x_W} v_{vs}[\theta - \theta_{bar}]dxdz + \int_{-H}^{0} \int_{x_E}^{x_W} v_{Ek}\theta_{Ek}dxdz \tag{5}$$

where θ_{bar} is the depth averaged potential temperature, and θ_{ek} follows the Ekman velocity definition, i.e., θ_{ek} assumes only two values over depth, one as the average in the Ekman layer, and another in the layer below the Ekman layer. Each of the terms in Equation (5) is considered a heat transport, because the velocity components are design to be compensated and allow zero net volume transport across the section (Hirschi et al. 2003).

5. Results

a. AMOC reconstruction

The AMOC strength calculated from the model output velocities in a 7-day average is highly variable in time (Figure 3a; black line), with amplitude from -8 to 35 Sv (1 Sv = 10^6 m^{3}s^{-1}), and strong high frequency variability as well as a defined annual cycle. The time averaged AMOC streamfunction (Figure 3b) shows positive (northward) values in the upper 3500 m, negative (southward) values underneath, and a pronounced

maximum at the depth of $\sim$ 1500 m, which characterizes the AMOC strength. The AMOC strength in the model is 15.1 $\pm$ 7.6 Sv, lower than the observed estimates of 17.9 $\pm$ 2.2 Sv (Dong et al. 2009), but within the uncertainty estimates. Other high resolution models, such as the OFES model (Dong et al. 2011), show a strong agreement to the AMOC strength value (15.0 $\pm$ 3.7 Sv) presented here.

The AMOC streamfunction is decomposed into its vertical shear, Ekman and barotropic components using the methodology described in Section 4a Therefore, each component is independently estimated, accordingly to Lee and Marotzke (1998) and Baehr et al. (2004), but differently from the methodologies of Perez et al. (2011) and Dong et al. (2011), which estimate the geostrophic transport either unbalanced for mass transport or as the residual between the total and Ekman transports. The absolute geostrophic component (barotropic plus vertical shear) is calculated by using a level of known motion at the bottom of the ocean, assuming that velocities are perfectly known there. The vertical shear component has the strongest contribution to the total AMOC strength, with an average of 26.9 $\pm$ 3.1 Sv, and it is in great part compensated by the barotropic contribution of the transport, which is negative (southward) with an average of -15.9 $\pm$ 6 Sv. The absolute geostrophic transport is therefore 11 $\pm$ 6.7 Sv, smaller than the observational value of 15.7 $\pm$ 2.6 Sv (Dong et al. 2009) and from the OFES model (12.9 $\pm$ 2.1 Sv; Dong et al. (2011)). Because here we use a different methodology and a different time range we cannot rule out the cause of these differences. It is worth mentioning that neither the barotropic nor the vertical shear streamfunctions show a reversal in depth, as observed on the total mean streamfunction, but the addition of the two streamfunctions produce the same reversal pattern at approximately 3500 m (magenta line in Figure 3c) due to their different depth behaviors. Strong interannual variability is observed in the barotropic component, with positive anomalies in the austral summer of 2007 and 2008 and negative anomalies in the austral spring of 2009 and 2010. The Ekman has the lowest contribution to the mean AMOC strength, only 2 $\pm$ 4 Sv, but its maximum amplitude can reach over 10 Sv, which is considerable in comparison to the other components.

The HT follows the same pattern as the AMOC (Figure 4). The mean HT calculated directly from the model fields is 0.33 $\pm$ 0.5 PW (1 PettaWatt = 10^{15}W), which is also lower than the values calculated from observational studies (0.54 $\pm$ 0.11 PW; Garzoli and Baringer (2007)). The barotropic HT component (-0.6 $\pm$ 0.23 PW) compensates in large extent the vertical shear component (0.8 $\pm$ 0.35 PW), and Ekman contributes about one third of the total HT (0.12 $\pm$ 0.24 PW).

The annual variability of the AMOC and HT components (Figure 5) show that the vertical shear component does not have a significant annual cycle. The Ekman and barotropic components have stronger annual cycles, and are approximately in phase with each other, with more positive values from March to August. This produces a total geostrophic transport (vertical shear plus barotropic) that is reasonably in phase with the Ekman component, a results that is at odds with previous observational studies (e.g., Dong et al. 2009),

which shows that the Ekman and geostrophic AMOC annual cycle cancel each other, producing no annual total AMOC variability. However, other high-resolution models also show a similar annual cycle for the total AMOC (e.g., Dong et al. 2011; Perez et al. 2011) as observed here. The residual contribution, which is the part of the annual variance that is not explained by the reconstruction (cyan line, Figure 5), is negligible for the AMOC but can be significant for the HT, especially during the austral summer when the model HT values are close to zero and its reconstruction is up to 0.5 PW. As observed in Figure 4a, the model HT is weak or sometimes negative during austral summer, and these reversals of HT are not featured in the reconstruction (Figure 4a, magenta line). These differences may be associated with unbalanced flow of volume (0.94 $\pm$ 3.8 Sv), whose HT contribution is here estimated as of -0.02 $\pm$ 0.06 PW, ageostrophic terms other then Ekman (Sime et al. 2006), and non-linearities in the HT calculation. Other methodologies also show a stronger reconstructed HT in comparison with the direct estimates from models (Perez et al. 2011). Surprisingly, the mean of the reconstructed HT, which is higher than the original timeseries, is of 0.54 PW, the same value as observed by Garzoli and Baringer (2007).

b. XBT observational strategy

The AX18 XBT transect, which was designed with the main purpose of monitoring the variability of the upper limb of the AMOC transport, measures temperature in the upper ocean ($\sim$ 800 m) between Cape Town and South America quarterly at a high-density (between 25-50 km) zonal spacing.

Previous observational studies that used AX18 observations to estimate meridional volume and heat transports performed several observational assumptions. The XBTs measure temperature profiles in the upper 800 m depth (e.g. Deep Blue probe type). Because XBTs do not measure salinity, a common method to infer salinity at the XBT temperature profile location uses a lookup table derived from historical temperature-salinity (T-S) relationships (Thacker 2008). Below 800 m depth, climatological temperature and salinity are applied down to the bottom of the ocean (Dong et al. 2009). The barotropic or external mode is generally estimated by adopting as a level of no motion at the depth where the potential density anomaly referenced to 2000 dbar assumes the value of 37.09 Kgm^{-3} (σ_2 = 37.09). The σ_2 = 37.09 depth is approximately located at 3700 m depth and between two water masses, the North Atlantic Deep Water (NADW) flowing southward between 1500 and 3700 m, and the underlying Antarctic Bottom Water (AABW) flowing northward (Ganachaud and Wunsch 2003; Baringer and Garzoli 2007). The Ekman component of the flow is calculated from available zonal wind stress products at the XBT deployment locations.

In order to simulate the XBT observations in the model, we make the same assumptions as used in the observational studies: i) the model temperature data are used above 800 m, ii) a quadratic least squared

fit between the annual mean temperature and salinity obtained from the model is specified for each depth, calculated using 1 degree boxes along 34°S, and iii) the monthly climatology of temperature and salinity at a 1 degree longitudinal resolution is padded below 800 m to extend the pseudo-observations to the bottom of the ocean and iv) a reference level for the velocity calculation is chosen. Constructing the T-S relationships from the model instead of using, for example, the World Ocean Atlas (WOA) climatology is necessary, since the model own internal biases relative to the observations could potentially bring spurious T-S discontinuities. WOA climatology is subject to biases in regional coverage, such as below 2000 m (the parking depth of Argo floats) or along coastal areas, and historically in the South Atlantic. Here, we do not account for imperfect sampling although its effects can be sizeable in producing additional seasonal biases.

The RMS error between the model salinity and the salinity estimated by the lookup table is shown in Figure 6. In the top 200 m, salinity errors associated with the T-S inference are of the order of 0.1 psu. Higher values are found in the western side of the basin ($\sim$ 0.4 psu) in the upper 100 m, where there is a fresh water inflow from river runoff. Below 200 m the RMS difference is generally lower than 0.1 psu, with higher values located around 500 m and decreasing to near zero below 1000 m. These error values are of the order of the annual RMS difference of salinity, and therefore are highly driven by the seasonal variation of T-S relationships, which is not captured by the annual mean T-S relationships.

It is also important to mention that XBT measurements do not contain pressure measurements, and estimate the depth following a quadratic fall rate equation (FRE) on the time of descent of the probe. The FRE is subject to a parametric uncertainties, which translate into depth biases to the XBT profile. Typical FRE biases are on the order 2% of depth (Goes et al. 2013b). We estimate the AMOC and HT errors associated with a typical FRE bias in the upper 800 m, and their values are -0.06 $\pm$ 0.07 Sv and -0.01 $\pm$ 0.01 PW, respectively.

c. AMOC and HT uncertainties due to the XBT transect observational sampling

In this section we investigate the uncertainties associated with each of the assumptions applied in the AX18 transport estimates. We focus on the four main assumptions of the AX18 design, which are i) temporal resolution, ii) horizontal resolution, iii) salinity and bottom temperature inferences, and iv) reference level for geostrophic velocity calculations. We apply each of the assumptions individually in order to quantify their uncertainties, which will allow recommending improvements for each assumption in the AX18 transect design.

1) Temporal resolution

The AX18 transect was originally implemented to be carried out four times a year. These measurements can produce snapshots of the geostrophic AMOC transport, and this rate of time sampling as well as the year-to-year variability of number of transects may alias the estimates of the annual cycle of the AMOC and meridional heat transport (Bryden et al. 2005). Uncertainties associated with the transect temporal sampling are simulated by randomly selecting snapshots of temperature and salinity sections, and differences in the geostrophic AMOC and HT are used as metrics for the uncertainty estimation. We reproduced this simulation 400 times, which is a number sufficiently high to allow the average of all realizations to have the same monthly means as the original model geostrophic AMOC and HT. Furthermore, the mean monthly RMS of the 400 realization will define a measure of the uncertainty associated with the time sampling. We vary the simulated number of the AX18 realizations per year from 1 to 20, and the number of years of data collection from 1 to 15. In order to simulate different number of years of data collection when they exceed six years (the total model simulation), we extend the original time series resampled stretches randomly selected for each the 400 simulations, choosing carefully the beginning of each stretch to keep the timeseries seasonality. Contour plots showing the sampling error variability of the AMOC and HT with respect to the number of years measured and the number of samples per year is shown in Figure 7. The time sampling error of the AMOC and HT show similar behavior, i.e., errors decrease exponentially as more samples are collected during the year or when a higher number of years are sampled. The RMS errors can be as low as 0.5 Sv and 0.05 PW when measuring up to 12 times per year for 15 years, or above 2.4 Sv and 0.25 PW had the transect been carried on only 2 times a year for 2 years. Using our selection of 18 sections of the AX18 transect along the nominal zonal transect of 34°S (Figure 2), and assuming a quarterly sampling, we can loosely approximate the number of years to five. The currently sampling is represented by a star in the considered parameter space in Figure 7, whose associated error values are 2.3 Sv for the AMOC and 0.24 PW for HT, close to the most uncertain values in the studied parameter space.

One additional temporal sampling error arises from the non-synopticity of the XBT transect measurements. The AX18 cruises take approximately 10 days to complete the trajectory from South America to Cape Town, which may alias the transport estimations across the transect. We quantify the errors due to non-synopticity by simulating the same observational assumption within the model environment. In this experiment (not shown), we use daily mode outputs to resample the profiles along the 34°S section such that each section spans over a 10-day long period. We then use 7-day outputs of the resampled AMOC and HT timeseries to compare with the original 7-day transports, which are chosen on the first day of each 10-day period. The errors associated with the non-synopticity of the data are 0.22 ± 4.2 Sv for the AMOC and

0.02 ± 0.24 PW for HT.

2) Horizontal sampling

The AX18 transect crosses regions of different regimes of meridional transport (Figure 1). Previous studies partition the transport into the western (Confluence region) and eastern (Agulhas) boundaries and interior (subtropical gyre), suggesting that it is critical to account for the variability in all three regions in order to monitor and quantify changes in the AMOC and MHT (Dong et al. 2009). The current XBT horizontal sampling strategy samples the basin at different rates according to regional characteristics, at a lower density ($\sim$ 50 km) in the interior region, and higher density ($\sim$ 25 km) closer to the boundaries, i.e., east of the Walvis Ridge ($\sim 1°$W) and west of 40°W, outside the continental slope region in South America. This is a heuristic approach to add more resolution to the boundaries, where higher energy is contained (Figure 1). Here we quantify the sensitivity of the meridional transport to the horizontal resolution in these three regions. We generate an ensemble with 30 members by degrading the longitudinal resolution in each of the three regions at a time, from the original 0.08 degree up to 5 degrees at variable steps, giving more focus on the high resolution sampling. We use the RMS error, bias and correlation as metrics to compare the reconstructed with the original AMOC and HT strength.

Our results show that the AMOC strength and HT are less sensitive to changes in the spatial resolution in the interior than at the boundary regions (Figure 8). For the AMOC, degrading the resolution in the interior produces a small negative bias and RMS error of -0.6 $\pm$ 1.5 Sv (i.e., bias $\pm$ RMS) at 5° longitude sampling, and reduces the correlation to $\sim$ 0.9 at this lowest sampling rate considered. In the boundary regions, where reducing spatial sampling is more effective to causing changes in the AMOC and HT, and the bias and RMS error for a 25 km spacing is of 2.8 $\pm$ 3.2 Sv in the western and 0.23 $\pm$ 1.2 Sv in the eastern boundary. The correlation is about 0.9 at 25 km in the boundaries, and decreases quickly to 0.6 when sampling is lower than 1° longitude. The stronger decrease of correlation in the boundaries is partly because of the strong currents and high mesoscale activity there, especially in the western part, and because of the shelf transport that can be completely misrepresented. At the western shelf ($<$ 1000 m), the model volume transport is mostly southward of -4.4 $\pm$ 2.4 Sv. In the eastern shelf, the transport is northward above 1000 m and east of 17.5°E is 1.5 $\pm$ 2.0 Sv. Both transports on the shelf contribute with a negligible temperature transport ($\sim 10^{-5}$ PW).

Interestingly, biases in the AMOC strength and HT have opposite signs and similar magnitudes when comparing the western and eastern boundaries for a given zonal sampling resolution (Figure 8c, f). Therefore, biases in the eastern and western regions cancel each other to some extent.

d. AMOC and HT uncertainties due to computational methodology

In the previous section we analyzed the sensitivity of the AMOC and HT to strategies for different temporal and spatial sampling of the XBT transect. In this section, we will investigate how methodological assumptions affect the AMOC and HT estimated at 34°S. First we will explore the impact of salinity and deep temperature inferences. Additionally we will optimize the choice of the reference level, and propose a method to estimate the barotropic velocities across the section.

1) Salinity and deep temperature inferences

To study the impact of salinity and deep temperature inferences on the AMOC and HT, we perform step changes in the model observational strategy. We compute PSIy and HT using: i) the constructed annual T-S lookup table (Section 5a) to estimate salinity profiles in the upper 800 m, ii) padding the model T-S monthly climatology in the deep ocean (> 800 m deep), and iii) using together the lookup table in the upper ocean and padding in the deeper ocean. We compare the changes in the geostrophic components of AMOC strength and HT to the one calculated with the total model fields (Figure 9). The AMOC residuals with respect to the total field show that the T-S lookup approximation drives most of the residual changes (-0.33 $\pm$ 2.6 Sv). Residuals from the T-S lookup approximation are subject to strong seasonality as observed during austral winter, when biases can reach almost -2 Sv. This is because here the T-S relationships are taken from an annual mean. Deep ocean padding shows only a small seasonality, and AMOC mean biases are small, of 0.06 $\pm$ 2.3 Sv. For the HT, padding and TS lookup residual changes, -0.03 $\pm$ 0.14 PW and 0.02 $\pm$ 0.16 PW, respectively, are of similar strength, and both show seasonality, although as for the AMOC, T-S lookup approximation controls to a large extent the residuals when both approximations are in place (0.02 $\pm$ 0.18 PW). Therefore, although both lookup table and padding approximations bring similar errors, the T-S lookup controls the seasonal variations in the AMOC and HT.

2) Reference level for absolute geostrophic velocities

The barotropic mode accounts for most of the bias of the overturning circulation contribution (Baehr et al. 2004). As indicated from the model output (Figure 10), variations in bottom topography are the main driver of strong bottom velocities, which increases the barotropic contribution and its potential biases as well. Zonal sections, where boundaries are steeper and more similar to a vertical wall, can reduce the effect of barotropic contribution (Rayner and Coauthors 2011). At 34°S, where there are strong bottom velocities, strong biases in the barotropic component could be introduced by assuming an inaccurate reference velocity (Equation

2). We estimate the sensitivity of the barotropic AMOC (PSI_{bar}) to the reference level by performing four experiments: a) with zero reference velocity, b) with climatological reference velocity at the western boundary, c) with climatological reference velocity at the eastern boundary, and d) with climatological velocity at both western and eastern boundaries. Similar to observational studies, we use in all experiments the reference depth at the σ_2 = 37.09. The evolution and the mean barotropic streamfunction are shown inFigure 11. The minimum barotropic streamfunction, which characterizes its strength, is located between 2 and 3 km deep. Using model velocities, the mean PSIbar strength is estimated as -16.26 Sv. When zero reference velocity is assumed, a much weaker value is estimated (PSI_{bar} = -9.26 Sv). Western and eastern boundary reference velocity contributions are similar, and the derived PSIbar strength estimates also have positive bias of 4.7± 2.2 Sv and 3.4 ± 1.8 Sv, respectively. When both eastern and western reference velocity are added, the mean PSIbar = -15.22 Sv, and the PSIbar strength is correctly measured at value of 1 ± 1 Sv. Therefore, the knowledge of the reference level velocities at both western and eastern is necessary for considerably reducing biases in the barotropic mode.

3) Alternative barotropic velocity estimation using altimetry and hydrography

In order to optimize the information necessary to monitor the AMOC at 34°S, several additional observations could be used to complement the AX18 XBT transect measurements. Some complimentary observations are already in place, such as the satellite wind stress measurements to estimate the Ekman transport.

A topic of current research in the AMOC decomposition is the estimation of the barotropic mode. Using a reference level near the bottom of the ocean cannot capture interannual or longer variability due to the presence of deep flows, since in this work climatology is assumed below 800 m. Bottom pressure (P_{bot}) recorders are a useful platform to compute the time varying reference level for the meridional geostrophic velocity, and therefore, estimate the non-steric component of the sea level height (SLH). Such a platform requires further investment in an array across the basin, and efforts are underway (Perez et al. 2011; Meinen et al. 2012). Some recent studies use a blend of altimetry and Argo parking velocity as the reference level or level of known motion to infer absolute geostrophic velocities (Willis and Fu 2008; Mielke et al. 2013; Goes et al. 2013a). However, because a large number of Argo floats is necessary to produce a reliable estimate, seasonal averages are generally used in an Argo-based reference level. We showed in the previous section that a climatological assumption of the reference velocity in the eastern and western boundaries can reduce the AMOC biases considerably. Here we test another method for measuring the barotropic flow by using SLH derived from satellite altimetry in conjunction with hydrographic data. Altimetry captures both steric and non-steric components, whose contributions are variable among different regions of the ocean (Guinehut et al.

2006). The non-steric contribution generally increases toward higher latitudes due to weaker stratification and stronger Coriolis force. In some regions the non-steric contributions, such as the barotropic component, can account for more than 50% of the total sea level variability (Shriver and Hurlburt 2000).

Using a hydrostatic relation, the non-steric sea level can be accurately related to bottom and atmospheric (Patm) pressure (Park and Watts 2005) as SLH = $(\mathrm{P}_{bot} - \rho_0 g H - P_{atm})/\rho_0 g$. In order to estimate the non-steric component of the sea level, we filter the steric contribution by calculating the residual between SLH and the dynamic height referenced at a certain level (SLH DH). The barotropic velocities are calculated using geostrophy on this residual field, and the maximum barotropic streamfunction calculated from these velocities is then compared to the model barotropic streamfunction.

We consider DH referenced at a certain depth, and estimate the optimal reference depth varying the reference of DH from 300 up to 3500 m deep (Figure 11c). According to our results, the structure of the variability of the barotropic velocities can be well captured by the non-steric sea level. The strength of the barotropic AMOC show correlations above 0.6 irrespective of the reference level used in the DH estimation. High correlations (> 0.9) are found for a DH reference level between 500 m and 1000 m. A minimum RMS region (< 5 Sv) overlaps with the maximum correlation region, and it is found for a reference level between 700-1100 m (Figure 11a), with a minimum of ~ 3 Sv referenced at 1000 m. Finally, we quantify how much information is gained by using altimetry data instead of using the $\sigma_2 = 37.09$ as the reference level for barotropic velocity. The barotropic streamfunction strength using the $\sigma_2 = 37.09$ reference level shows RMS error and correlation of 9 Sv and 0.78, respectively. Using altimetry and DH referenced at 800 m, the maximum depth of an XBT profile, promotes a gain of 4 Sv in RMS and 0.15 in correlation towards this density reference level.

6. Conclusion

In this study we use a high resolution model assimilation product to assess the observational and computational uncertainties associated with estimating meridional transports using the data from the AX18 XBT transect along 34°S. The results obtained here are summarized in Table 1. As follows, we make recommendations for optimization of sampling and computational methodologies to improveme estimates of the AMOC and meridional HT:

- The effect of T-S padding from monthly climatology below 800 m on the AMOC (0.06 ± 2.6 Sv) and HT (-0.03 ± 0.14) estimates is small in comparison to the other error sources. This is is a conservative estimate given that the model climatology represents well the variability below the surface. The salinity

from the T-S lookup table in the upper 800 m is also small in comparison to other components, and about the same order as the deep ocean padding. However, due to seasonal biases, monthly biases can reach 2 Sv. Salinity from other measurements such as Argo, or monthly climatology T-S relationships would avoid seasonal biases.

- Current quarterly sampling causes an average RMS error of 2.3 Sv and 0.24 PW in the climatological AMOC and HT estimates, respectively. The optimal strategy to reduce this sampling error would be to carry out 12 transects per year, i.e. one per month, which is subject to operational constraints. More realistically, it is desirable to conduct continuous realizations at current quarterly sampling for at least 15 years.

- Spatial subsampling in the interior produces small errors in the AMOC and HT estimates compared to the errors produced at the boundaries. The current AX18 zonal sampling uses 25 km on the boundaries and 50 km in the interior of the basin. This strategy seems to be adequate to capture most of the variability of the meridional transports. An increase in the boundaries sampling to 20 km would improve current AMOC results, since it would capture better the variability of the shelf transport.

- As described in previous studies (e.g., Kanzow et al. 2007, for 26.5°N), the barotropic is likely to be the strongest source of errors in AMOC and HT due to an extense continental shelf along 34°S. Using climatological values as the reference velocities i nthe boundaries can reduce the AMOC bias to $\sim$ 1 Sv.

- The use of satellite altimetry observations in conjunction with hydrographic data is a good alternative for barotropic term estimation. We show that barotropic volume transport estimates using the non-steric component of altimetry can improve the RMS error in $\sim$ 3 Sv in comparison to the commonly used leel of no motion at σ_2 =37.09 kgm^{-3}.

Acknowledgments.

The authors want to thank Joe Metzger for providing the GLBa0.08/74.2 simulation output, and the ship companies Evergeen Lines, CMA CGM Lines, Hamburg Sud and Monte Azul for carrying out the AX18 cruises as part of the Ships of Opportunity project. This research was accomplished under the auspices of the Cooperative Institute for Marine and Atmospheric Studies (CIMAS), a cooperative institute of the University of Miami and the National Oceanic and Atmospheric Administration, cooperative agreement #NA17RJ1226, and was partly funded by the NOAA Climate Program Office.

REFERENCES

Baehr, J., J. Hirschi, J.-O. Beismann, and J. Marotzke, 2004: Monitoring the meridional overturning circulation in the North Atlantic: A model-based array design study. *J. Mar. Res.*, **62 (3)**, 283–312.

Baehr, J., D. McInerney, K. Keller, and J. Marotzke, 2008: Optimization of an observing system design for the North Atlantic meridional overturning circulation. *Journal of Atmospheric and Oceanic Technology*, **25 (4)**, 625–634.

Baringer, M. and S. Garzoli, 2007: Meridional heat transport determined with expendable bathythermographs, Part I: Error estimates from model and hydrographic data. *Deep-Sea Res. I*, **54(8)**, 1390–1401.

Beal, L. M., W. P. M. D. Ruijter, A. Biastoch, R. Zahn, and S. W. G. 136, 2011: On the role of the Agulhas system in ocean circulation and climate. *Nature*, **472, (7344)**, 429–436, doi:10.1038/nature09983.

Biastoch, A., C. W. B oning, F. U. Schwarzkopf, and J. R. E. Lutjeharms, 2009: Increase in Agulhas leakage due to poleward shift in the southern hemisphere westerlies. *Nature*, **462**, 495–498, doi:10.1038/nature08519.

Bryden, H. L., H. R. Longworth, and S. A. Cunningham, 2005: Slowing of the Atlantic meridional overturning circulation at 25°n. *Nature*, **438**, 655–657.

Chassignet, E., et al., 2009: U.S. GODAE: Global ocean prediction with the hybrid coordinate ocean model (HYCOM). *Oceanography*, **22(2)**, 64–75.

Cummings, J. A., 2005: Operational multivariate ocean data assimilation. *Quart. J. Royal Met. Soc., Part C*, **131(613)**, 3583–3604.

Dong, S., S. Garzoli, and M. Baringer, 2011: The role of interocean exchanges on decadal variations of the meridional heat transport in the South Atlantic. *J. Phys. Oceanogr.*, **41**, 1498–1511, doi:http://dx.doi.org/10.1175/2011JPO4549.1.

Dong, S., S. L. Garzoli, M. O. Baringer, C. S. Meinen, and G. J. Goni, 2009: Interannual variations in the Atlantic meridional overturning circulation and its relationship with the net northward heat transport in the South Atlantic. *Geophys. Res. Lett.*, **36**, L20 606, doi:10.1029/2009GL039356.

461 Donners, J. and S. S. Drijfhout, 2004: The lagrangian view of South Atlantic interocean exchange in a
462 global ocean model compared with inverse model results. *J. Phys. Oceanogr.*, **34**, 1019–1035, doi:http:
463 //dx.doi.org/10.1175/1520-0485(2004)034⟨1019:TLVOSA⟩2.0.CO;2.

464 Ducet, N., P.-Y. L. Traon, and G. Reverdin, 2000: Global high resolution mapping of ocean circulation from
465 Topex/Poseidon and ERS-1 and -2. *J. Geophys. Res.*, **105 (C8)**, 19 477–19 498.

466 Fox, D., W. J. Teague, C. N. Barron, M. R. Carnes, and C. M. Lee, 2002: The modular ocean data
467 assimilation system (MODAS). *J. Atmos. Ocean. Technol.*, **19**, 240–252.

468 Ganachaud, A. and C. Wunsch, 2003: Large scale ocean heat and freshwater transports during the World
469 Ocean Circulation Experiment. *J. Climate*, **16**, 696–705.

470 Garzoli, S. and M. Baringer, 2007: Meridional heat transport determined with expendable bathythermo-
471 graphs. Part II: South Atlantic transport. *Deep-Sea Res. I*, **54**, 1402–1420.

472 Garzoli, S., M. Baringer, S. Dong, R. Perez, and Q. Yao, 2012: South Atlantic meridional fluxes. *Deep-Sea*
473 *Res. I*, **71**, 21–32, doi:10.1016/j.dsr.2012.09.003.

474 Goes, M., G. Goni, V. Hormann, and R. Perez, 2013a: Variability of the Atlantic off-equatorial eastward
475 currents during 1993-2010 using a synthetic method. *J. Geophys. Res.-Oceans*, **118 (6)**, 3026 – 3045,
476 doi:10.1002/jgrc.20186.

477 Goes, M., G. Goni, and K. Keller, 2013b: Reducing biases in xbt measurements by including discrete
478 information from pressure switches. *J. Atmos. Oceanic Technol.*, **30**, 810–824, doi:http://dx.doi.org/10.
479 1175/JTECH-D-12-00126.1.

480 Goni, G., F. Bringas, and P. D. Nezio, 2011: Observed low frequency variability of the Brazil Current front.
481 *J. Geophys. Res.*, **116**, C10 037, doi:10.1029/2011JC007198.

482 Goni, G., S. Garzoli, A. Roubicek, D. Olson, and O. Brown, 1997: Agulhas ring dynamics from
483 TOPEX/POSEIDON satellite altimeter data. *Journal of Marine Research*, **55(5)**, 861–883.

484 Goni, G. and I. Wainer, 2001: Investigation of the Brazil Current front variability from altimeter data. *J.*
485 *Geophys. Res.*, **106**, 31 117–31 128.

486 Gordon, A., 1986: Interocean exchange of thermocline water. *J. Geophys. Res.*, **91**, 5037–5046.

487 Griffies, S. M., M. J. Harrison, R. C. Pacanowski, and A. Rosati, 2004: A technical guide to MOM4. *GFDL*
488 *Ocean Group Technical Report No. 5, Princeton, NJ:: NOAA/GFDL*, 342 pp.

Guinehut, S., P.-Y. L. Traon, and G. Larnicol, 2006: What can we learn from global altimetry/hydrography comparisons? *Geophys. Res. Lett.*, **33**, L10 604, doi:10.1029/2005GL0255551.

Hall, M. M. and H. L. Bryden, 1982: Direct estimates and mechanisms of ocean heat transport. *Deep-Sea Res.*, **29**, 339–359.

Hawkings, E., R. S. Smith, L. C. Allison, J. M. Gregory, T. J. Woollings, H. Pohlmann, and B. de Cuevas, 2011: Bistability of the Atlantic overturning circulation in a global climate model and links to ocean freshwater transport. *Geophys Res Lett.*, **38**, L10 605, doi:10.1029/2011GL047208.

Hirschi, J., J. Baehr, J. Marotzke, J. Stark, S. Cunningham, and J.-O. Beismann, 2003: A monitoring design for the Atlantic meridional overturning circulation. *Geophysical Research Letters*, **30**, 1413, doi: 10.1029/2002GL016776.

Jayne, S. R. and J. Marotzke, 2001: The dynamics of ocean heat transport variability. *Reviews of Geophysics*, **39**, 385–411.

Kanzow, T., et al., 2007: Observed flow compensation associated with the MOC at 26.5 degrees N in the Atlantic. *Science*, **317(5840)**, 938–941.

Lee, T. and J. Marotzke, 1998: Seasonal cycles of meridional overturning and heat transport of the Indian Ocean. *J. Phys. Oceanogr.*, **28**, 923–943.

Lentini, C., G. Goni, and D. Olson, 2006: Investigation of Brazil Current rings in the confluence region. *J. Geophys. Res.*, **111(C6):C06013**, doi:10.1029/2005JC002988.

Locarnini, R. A., A. V. Mishonov, J. I. Antonov, T. P. Boyer, and H. E. Garcia, 2006: World Ocean Atlas 2005, Volume 1: Temperature. *NOAA Atlas NESDIS 61, U.S. Government Printing Office, Washington, D.C.*, 182 pp.

Meinen, C. S., A. R. Piola, R. C. Perez, and S. L. Garzoli, 2012: Deep Western Boundary Current transport variability in the South Atlantic: preliminary results from a pilot array at 34.5° S. *Ocean Sci. Discuss.*, **9**, 977–1008, doi:10.5194/osd-9-977-2012.

Mielke, C., E. Frajka-Williams, and J. Baehr, 2013: Observed and simulated variability of the AMOC at 26N and 41N. *Geophysical Research Letters*, **40(6)**, 1159–1164.

Park, J.-H. and D. R. Watts, 2005: Response of the southwestern Japan/East Sea to the atmospheric pressure. *Deep-Sea Res. II*, **52**, 1671–1683.

Perez, R. C., S. L. Garzoli, C. Meinen, and R. P. Matano, 2011: Geostrophic velocity measurement techniques for the meridional overturning circulation and meridional heat transport in the South Atlantic. *J. Atmos. and Ocean. Tech.*, **28, 11**, 1504–1521, doi:10.1175/JTECH-D-11-00058.1.

Pond, S. and G. Pickard, 1983: *Introductory Dynamical Oceanography*. Pergamon international library of science, technology, engineering and social studies, Butterworth-Heinemann, URL `http://books.google.com/books?id=5pQf8dBYxIUC`.

Rahmstorf, S., 1996: On the freshwater forcing and transport of the Atlantic thermohaline circulation. *Clim. Dyn.*, **12**, 799–811.

Rayner, D. and Coauthors, 2011: Monitoring the Atlantic meridional overturning circulation. *Deep-Sea Res. II*, **58**, 1744–1753.

Shriver, J. F. and H. E. Hurlburt, 2000: The effect of upper ocean eddies on the non-steric contribution to the barotropic mode. *Geophys. Res. Lett.*, **27**, 2713–2716, doi:10.1029/1999GL011105.

Sime, L. C., D. P. Stevens, K. J. Heywood, and K. I. Oliver, 2006: A decomposition of the atlantic meridional overturning. *Journal of Physical Oceanography*, **36 (12)**, 2253–2270, doi:10.1175/JPO2974.1.

Stramma, L. and M. England, 1999: On the water masses and mean circulation of the South Atlantic Ocean. *J. Geophys. Res.*, **104(C9)**, 20 863–20 883, doi:10.1029/1999JC900139.

Thacker, W. C., 2008: Estimating salinity between 25° and 45°S in the atlantic ocean using local regression. *J. Atmos. Ocean. Tech.*, **25**, 114–130, doi:10.1175/2007JTECHO530.1.

Treguier, A. M., M. England, S. R. Rintoul, G. Madec, J. L. Sommer, and J.-M. Molines, 2007: Southern Ocean overturning across streamlines in an eddying simulation of the Antarctic circumpolar current. *Ocean Sci.*, **3**, 491–507.

Wainer, I., P. Gent, and G. Goni, 2000: Annual cycle of the Brazil-Malvinas confluence region in the National Center for Atmospheric Research climate system model. *J. Geophys. Res.*, **05(C11)**, 26,167–26,177.

Weijer, W., W. P. M. D. Ruijter, H. A. Dijkstra, and P. J. van Leeuwen, 1999: Impact of interbasin exchange on the Atlantic overturning circulation. *J. Phys. Oceanogr.*, **29**, 2266–2284.

Willis, J. and L.-L. Fu, 2008: Combining altimeter and subsurface float data to estimate the time-averaged circulation in the upper ocean. *J. Geophys. Res.*, **113, C12**, 2156–2202, doi:10.1029/2007JC004690.

Zhang, R. and T. L. Delworth, 2005: Simulated tropical response to a substantial weakening of the Atlantic thermohaline circulation. *J. Clim.*, **18**, 18531860.

7. Figures and tables

List of Tables

TABLE 1. Bias ± RMS error of the AMOC (Sv) and HT (PW) introduced by each source of error associated with the AX18 XBT transect observational assumptions estimated in the present study. Last column shows the error estimates of Baringer and Garzoli (2007)

Source	AMOC (Sv)	Meridional Heat Transport (PW)	
	Present	Present	B&G
Upper ocean salinity	-0.33± 2.6	0.02 ± 0.16	0.03
Deep climatology below 800 m	0.06 ± 2.3	-0.03 ± 0.14	0.15
Mass imbalance	0.9 ± 3.8	-0.02 ± 0.06	0.02
Non-synopticity	0.22 ± 4.2	0.02 ± 0.24	–
Fall rate equation error (2% of depth)	-0.06 ±0.07	-0.01±0.01	–
Quarterly sampling	± 2.3	± 0.24	–
Unresolved western shelf transport	-4.4 ± 2.4	10^{-5}	0.01
Unresolved eastern shelf transport	1.5 ± 2.0	10^{-5}	0.01
Western Horizontal resolution	2.8 ± 3.2	0.13 ± 0.14	–
Eastern Horizontal resolution	0.2 ± 1.2	0.02 ± 0.04	–
Interior Horizontal resolution	-0.4 ± 1.0	0.06 ± 0.07	–
Western Reference level	4.7 ± 2.2	0.06 ± 0.08	0.05
Eastern Reference level	3.4 ± 1.8	0.10 ± 0.03	0.05

List of Figures

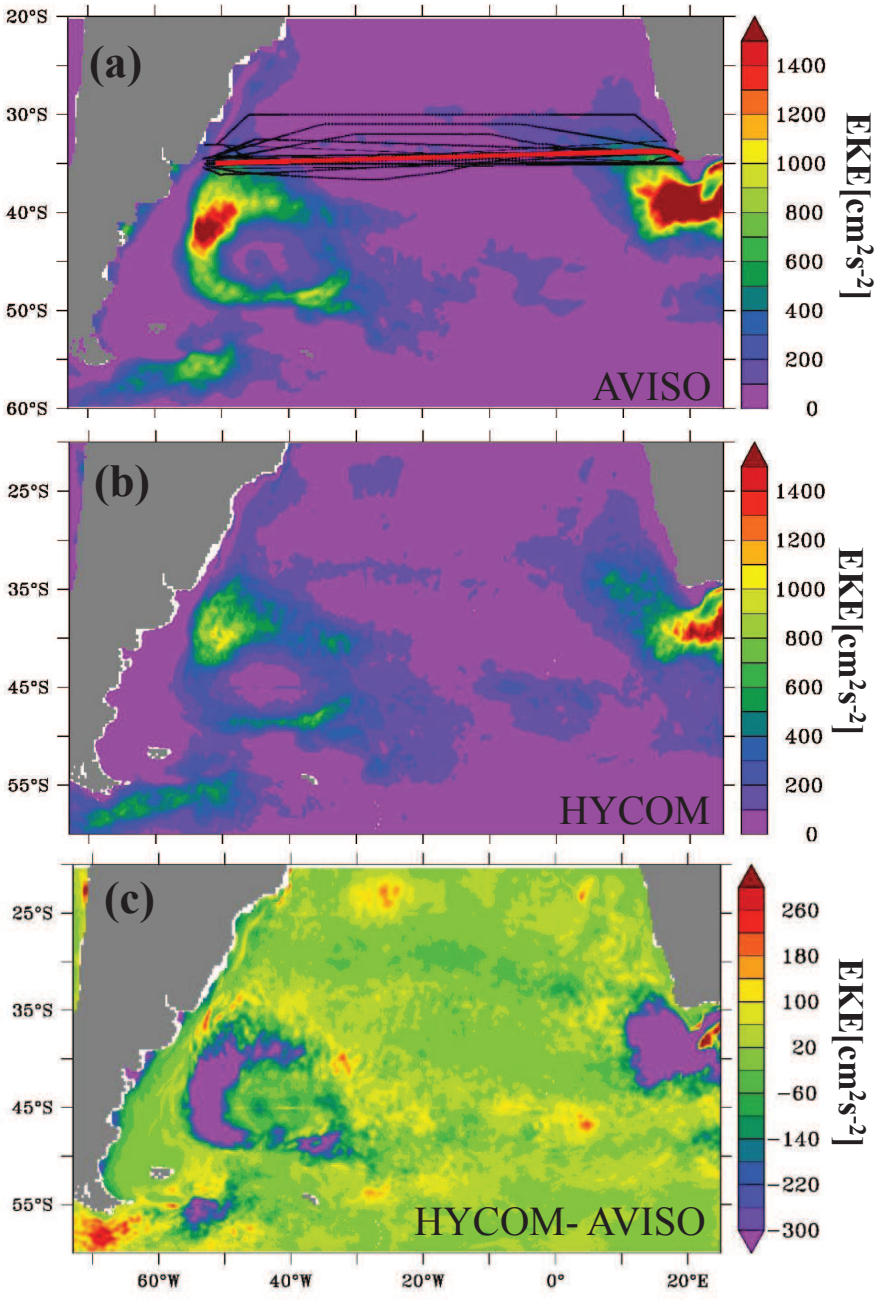

FIG. 1. Eddy kinetic energy (cm2 s^{-2}) calculated from sea level anomalies for the period between 2007 and 2013. (a) AVISO observations, (b) HYCOM model and (c) HYCOM minus observations. The black lines in Figure 1a are the locations of the 18 selected AX18 transects between **2002 and 2012**, overlaid by the mean AX18 transect location in red.

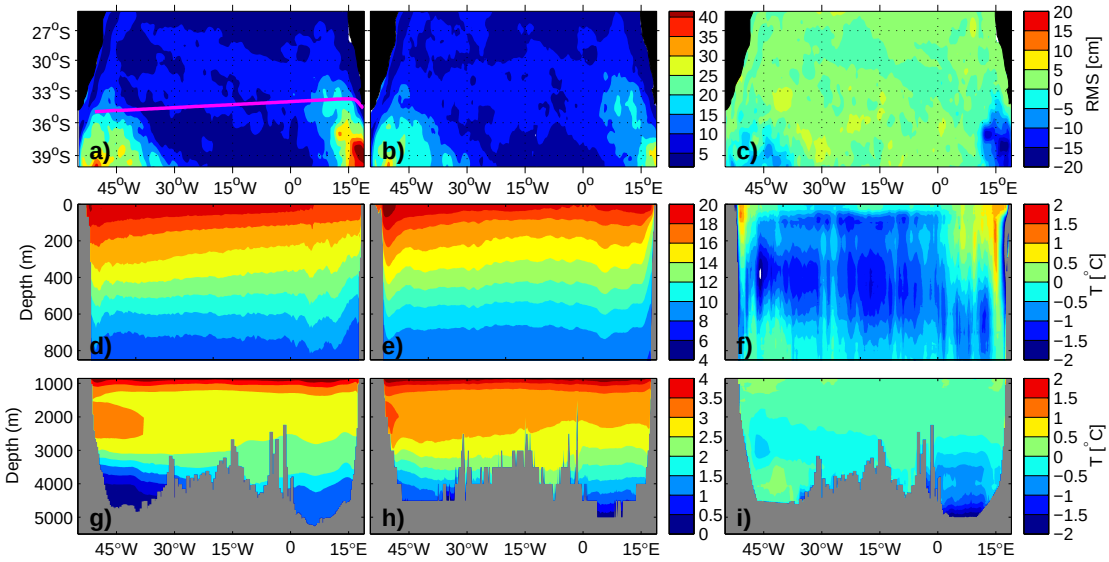

FIG. 2. (a) – (c): sea level anomaly (SLA) root-mean-square (RMS) contours (in cm) for.(a) AVISO overlaid by the mean AX18 transect (magenta); (b) HYCOM/NCODA and (c) HYCOM/NCODA minus AVISO. (d) (i): Mean temperature sections contours (in °C) for the (d, g) observations, with AX18 data for the upper 850 m (d) and WOA05 for 850m to bottom (g); HYCOM/NCODA model (e, g), and the HYCOM/NCODA minus observations (f, i).

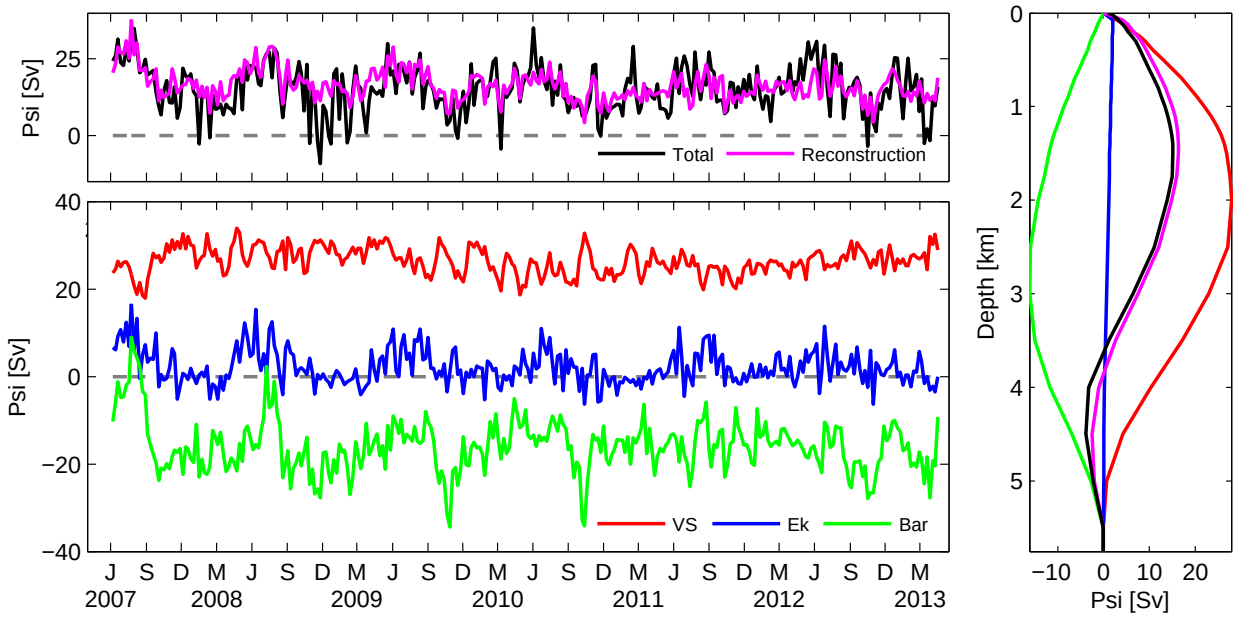

FIG. 3. a) Maximum volume transport streamfunction (AMOC) using model velocities (black) and the reconstruction (magenta). b) AMOC decomposition into vertical shear (red), Ekman (blue), and barotropic (green) components. c) Time mean meridional transport streamfunction for the model velocities (black), reconstruction (magenta), Ekman (blue), vertical shear (red) and barotropic (green).

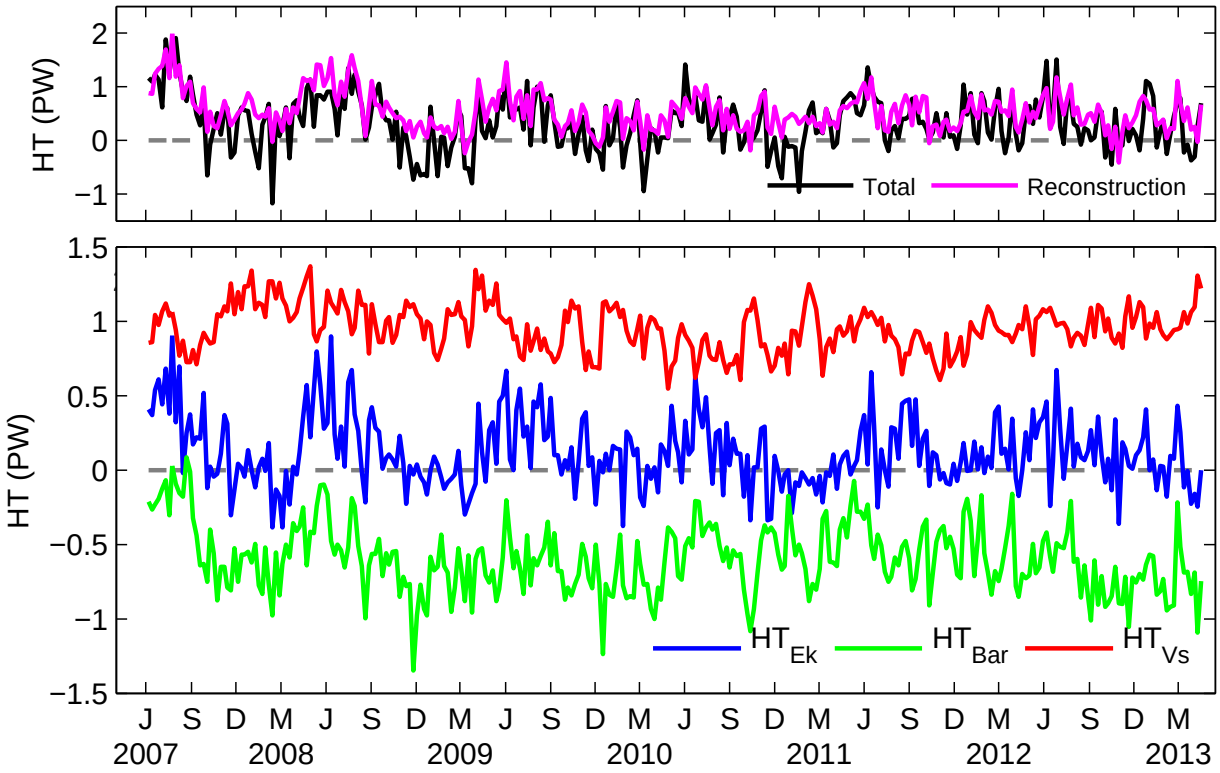

FIG. 4. a) Heat transport (HT in petaWatts) using model velocities (black) and reconstruction (magenta). b) HT decomposition into vertical shear (red), Ekman (blue), and barotropic (green) components.

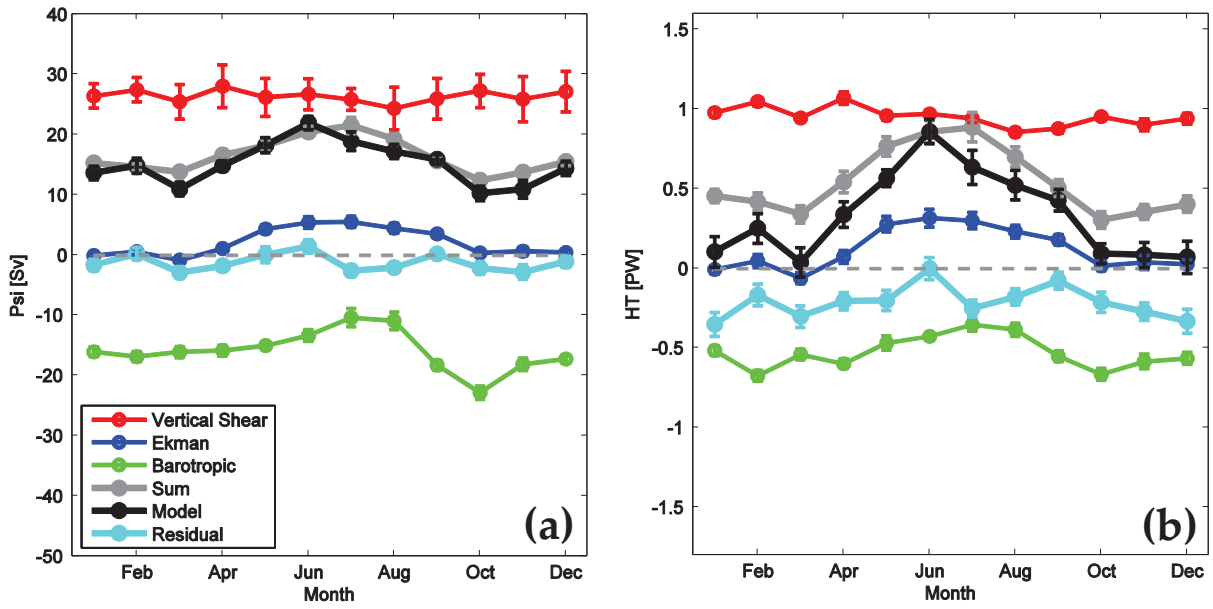

FIG. 5. Monthly means of the (a) AMOC and (b) HT components: vertical shear (red), Ekman (blue) and barotropic (green). The level of reference is assumed to be on the ocean bottom using the model bottom velocities as the reference. The sum of the transport components (grey) is comparable to the total transport from the original model velocities (black).

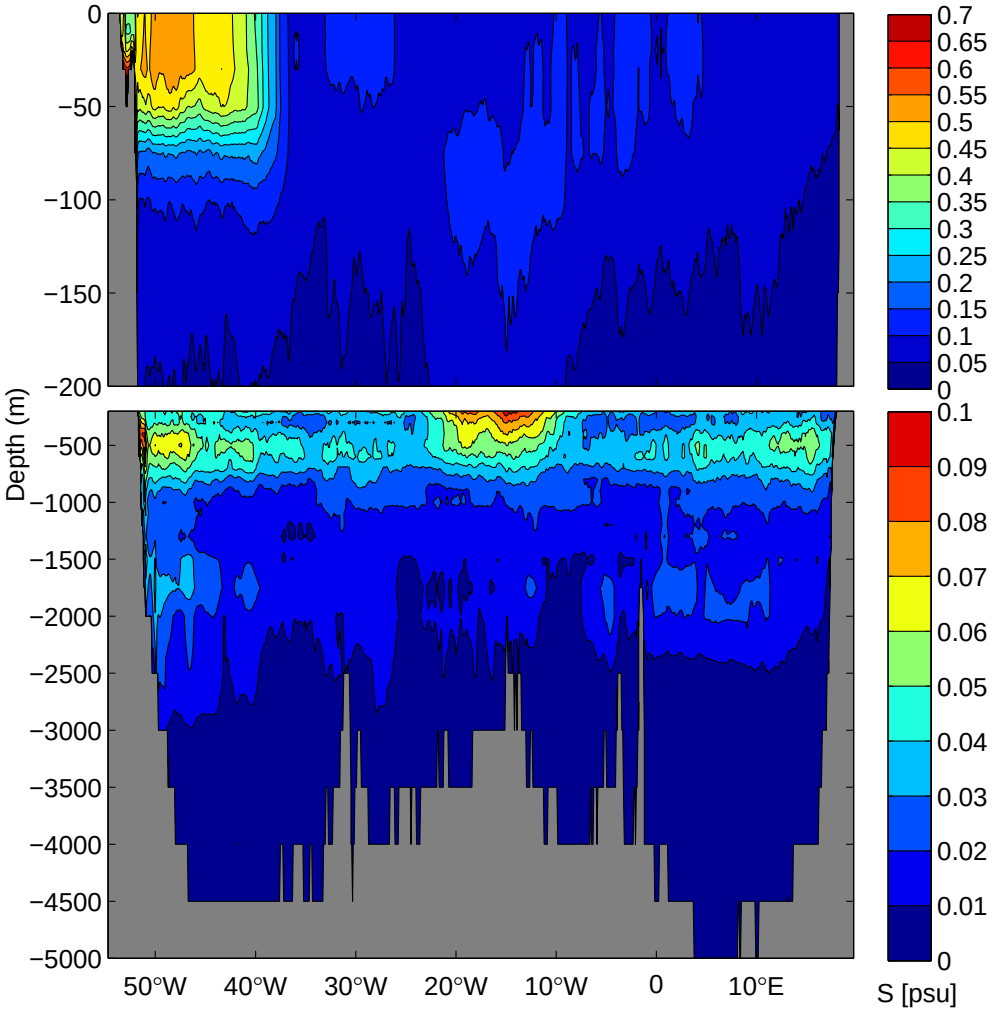

FIG. 6. RMS error between the estimated salinity using climatological T-S relationships and the model salinity along the 34.5°S section.

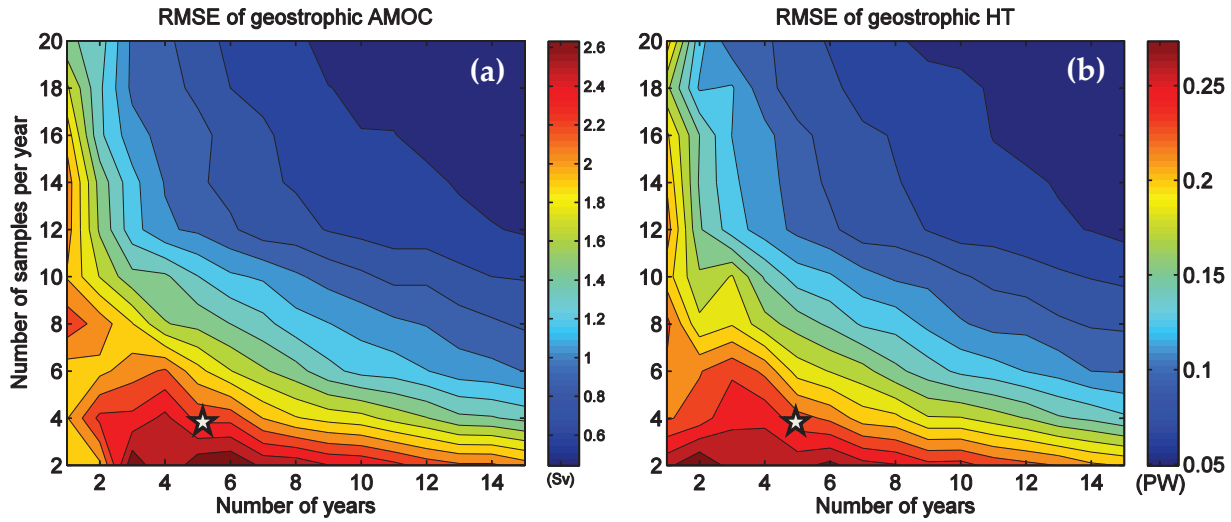

FIG. 7. RMS error of geostrophic AMOC (a) and HT (b) associated with different time samplings, i.e., the number of samples per year (y-axis) and the number of year (x-axis). The RMS error is calculated from the difference between the reconstructed timeseries using a different time sampling and the reconstructed timeseries using the original model sampling. The number of samples per year is randomly selected, and this process is realized 400 times to average the random realizations. The stars in (a) and (b) correspond to the current location of the AX18 sampling in the time sampling parameter space.

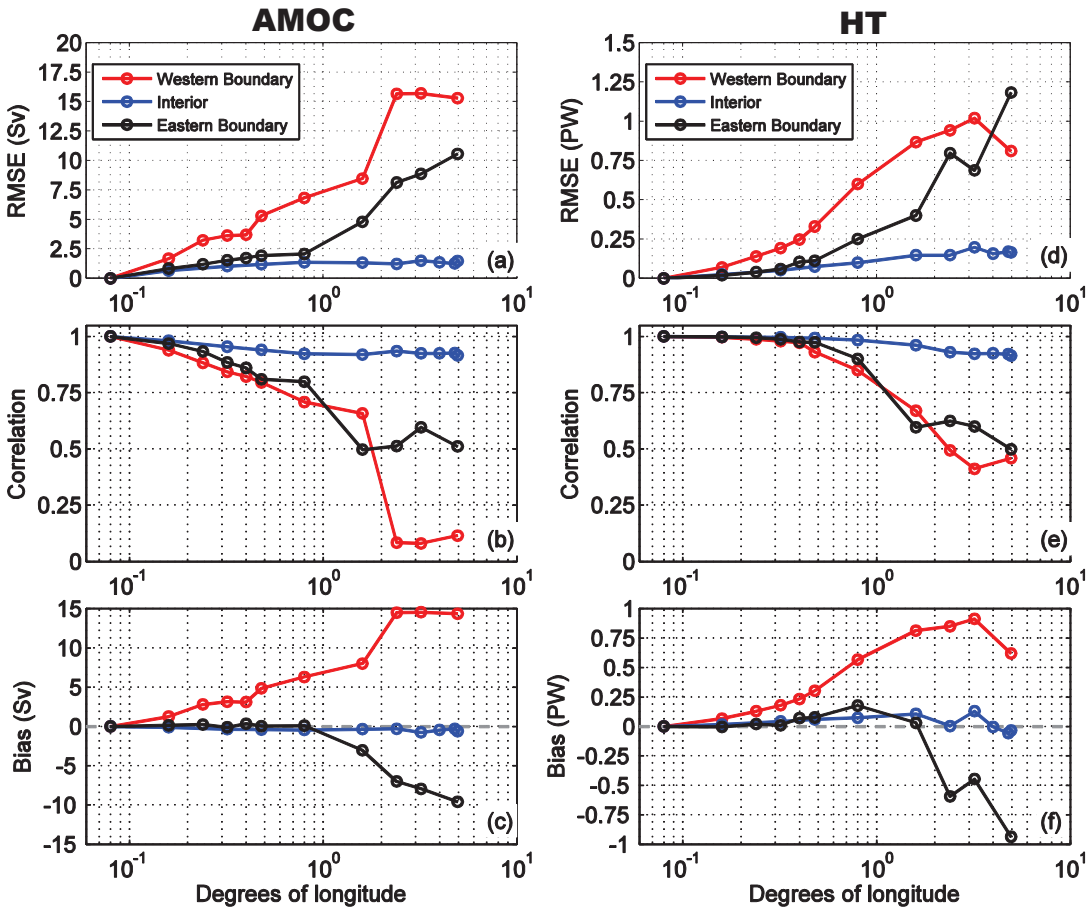

FIG. 8. RMS error, correlation, and bias of the AMOC (a, b, c) and HT (d, e, f) with respect to the simulated longitudinal resolution (in degrees) of the AX18 transect. The transect horizontal resolution varies individually for three regions, western boundary (red), interior (blue) and eastern boundary (black). The x-axis is shown in logarithmic scale.

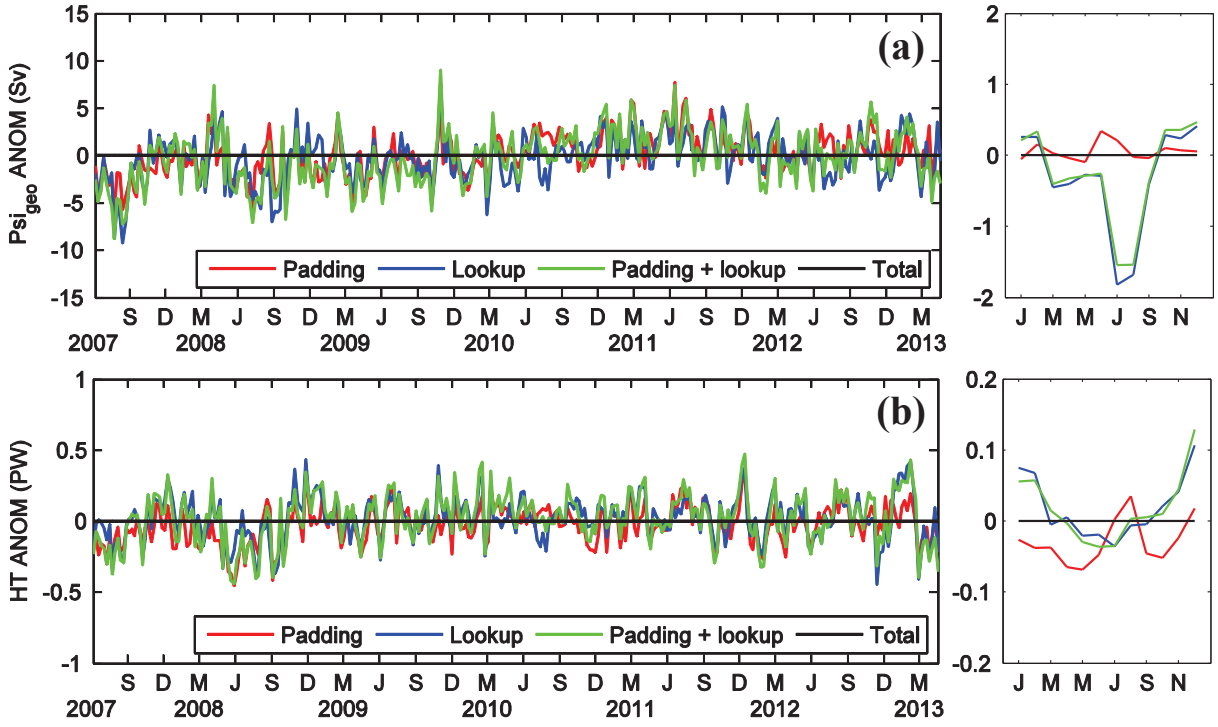

FIG. 9. Anomalies relative to the total model field timeseries of (a) geostrophic AMOC and (b) HT, and respective monthly averages (right panels). The total field anomalies is defined as having zero value (black), and the colored timeseries assume a bottom T-S climatology padding (red), salinity inference from lookup table in the top 800m (blue), padding plus T-S lookup (green) and the total (black).

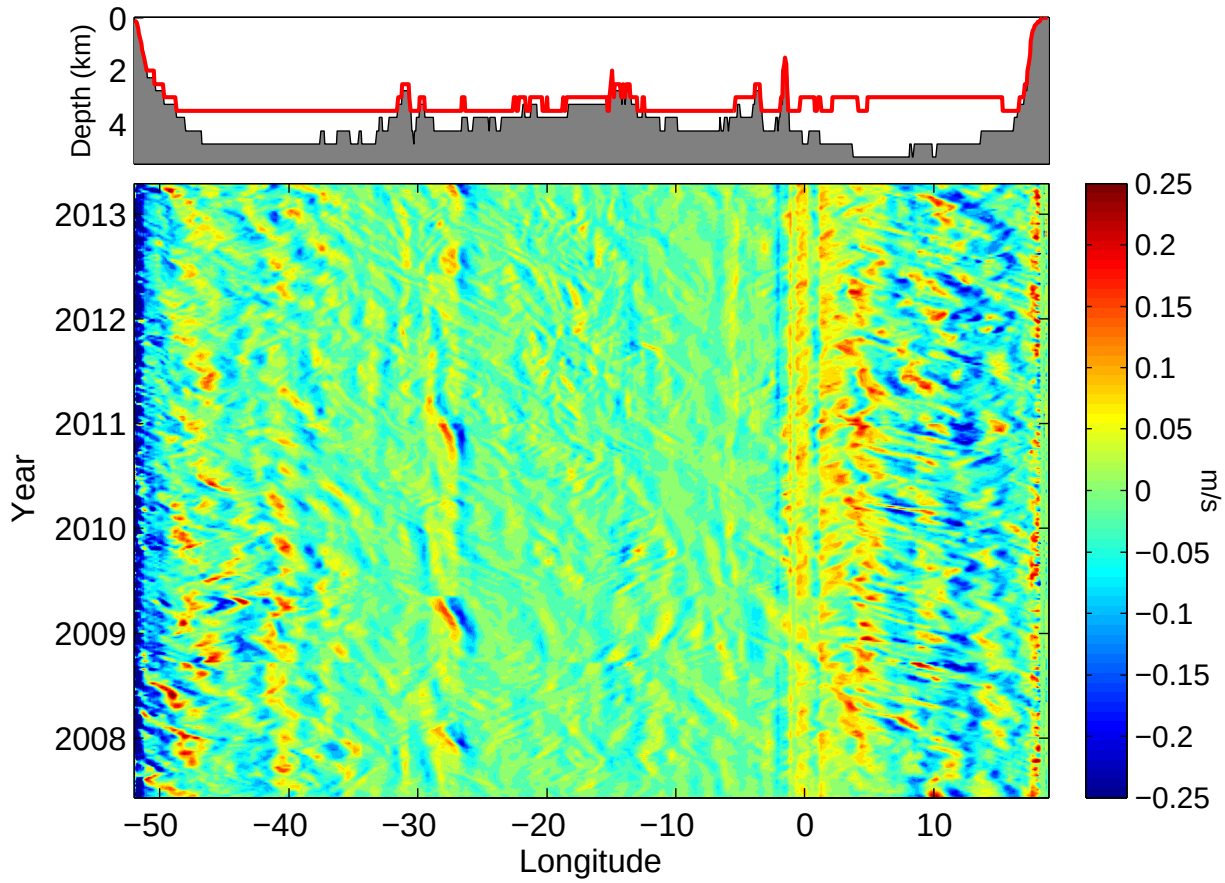

FIG. 10. Barotropic velocities at 34.5°S estimated from the model velocities. The top panel shows the depth if the average $\sigma_2 = 37.9$ (red line) overlaid on model bathymetry

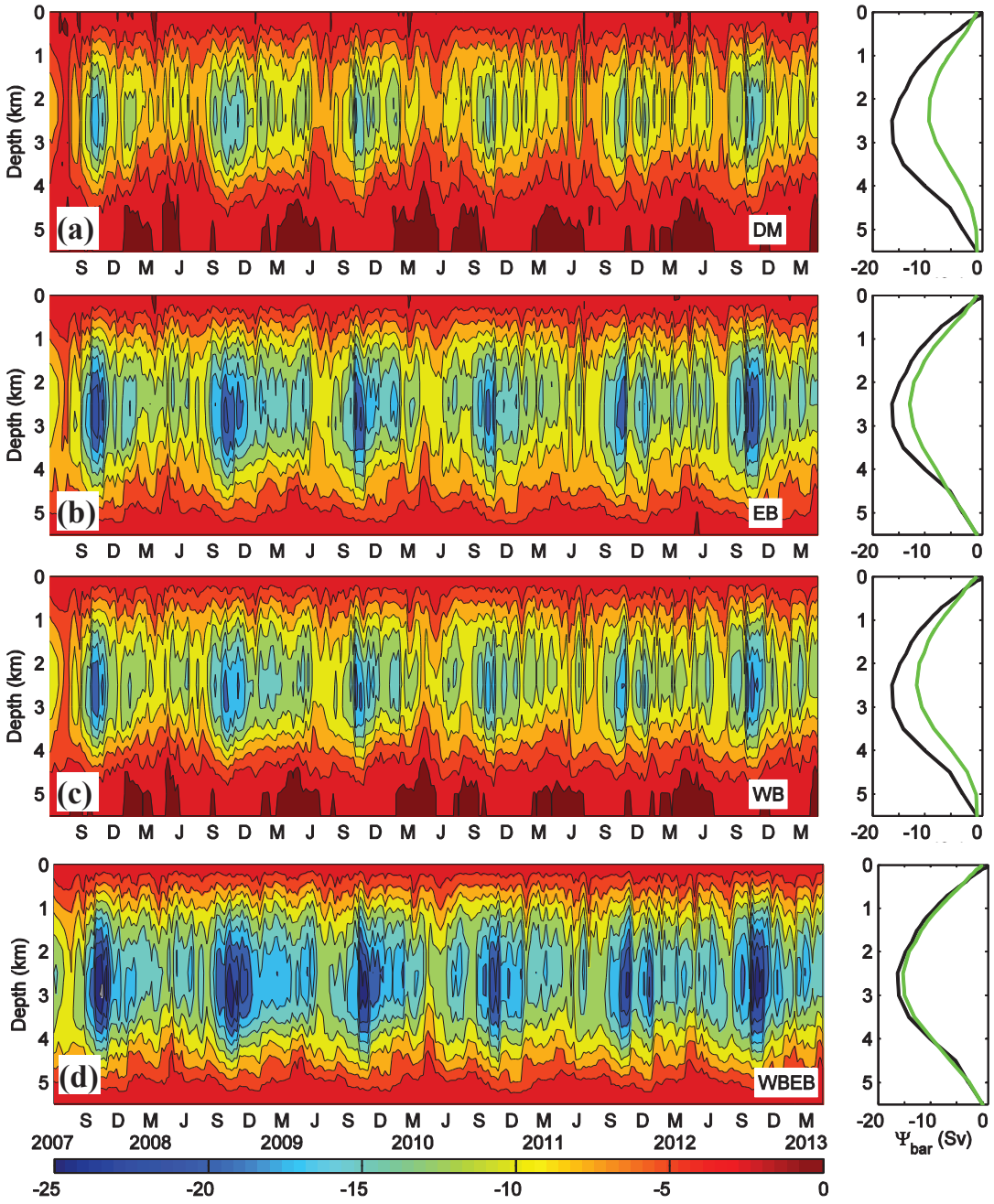

FIG. 11. Changes in the barotropic streamfunction (Sv) due to the knowledge of a climatological reference velocity at $\sigma_2 = 37.09$. (a) Zero reference velocity, (b) eastern boundary, (c) western boundary, and (d) western plus eastern boundaries. Left panels: time evolution of the barotropic streamfunction. Right panels: respective time average of the barotropic streamfunction.

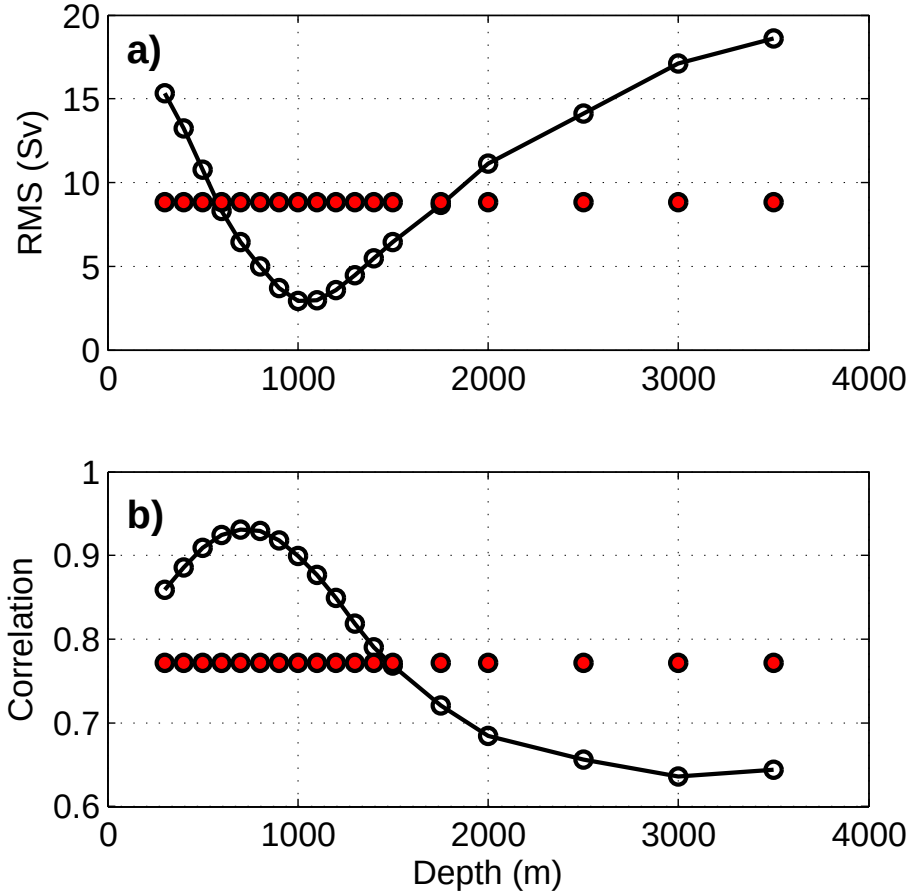

FIG. 12. a) RMS error and (b) correlation between the barotropic streamfunction strength for the barotropic velocities calculated from the SLH-DH residual with a variable reference level from 300 m to 3500 m depth (x-axis). Also added for comparison the RMS and correlation of the streamfunction strength for barotropic velocities calculated using a reference at level of no motion at $\sigma_2 = 37.09$ kg m^{-3}.